Prediction of airflow and heat transfer in a mechanically ventilated room with Large-Eddy Simulations based on Lattice Boltzmann Method

Teddy Gresse, Lucie Merlier, Jérôme Jacob, Frédéric Kuznik

Prediction of airflow and heat transfer in a mechanically ventilated room with Large-Eddy Simulations based on Lattice Boltzmann Method

Teddy Gresse[a,*], Lucie Merlier[a], Jérôme Jacob[b], Frédéric Kuznik[c]

[a] *Univ Lyon, UCBL, INSA Lyon, CNRS, CETHIL, UMR5008, Villeurbanne, F-69621, France*
[b] *Aix Marseille Univ, CNRS, Centrale Marseille, M2P2, UMR 7340, Marseille, 13451, France*
[c] *Univ Lyon, INSA Lyon, CNRS, CETHIL, UMR5008, Villeurbanne, F-69621, France*

Abstract

Conditioned airflows in mechanically ventilated rooms are characterized by a combination of complex features such as interaction or impingement with walls, buoyancy near a surface or a flow at a different temperature. The associated flow regimes can be either laminar, transient, or turbulent. Modeling these flows and the associated heat transfers at walls is therefore challenging, but is of the utmost importance for predicting building thermal behavior, thermal comfort, and ventilation efficiency.

This study aims to evaluate the capacity of a Large-Eddy Simulation (LES) approach using the Lattice Boltzmann Method (LBM) with adapted wall modeling to simulate axisymmetric and thermal jets generated by an air diffuser of complex design and developing near the ceiling of a full-scale test

*Postal adress: Bâtiment Sadi-Carnot, 9, rue de la Physique, Campus LyonTech La Doua, 69621 Villeurbanne cedex France

Email address: teddy.gresse@insa-lyon.fr (Teddy Gresse)

room. Simulation results are compared with detailed experimental data for the cases of an isothermal jet, a hot jet, and a cold jet in terms of mean velocity, temperature, and turbulence intensity profiles. The jet turbulence distribution is further analyzed by means of anisotropic invariant mapping and vortex visualization.

The results show good qualitative and quantitative agreement between simulation results and experimental data. In particular, the simulated velocity and temperature profiles within the jets are consistent with measurements, and the air temperature in the room's central occupancy region is correctly estimated. Also, the main turbulent mechanisms in the jets' development zone are well captured. Thus, the chosen approach enables detailed, high-fidelity simulations of airflow and heat transfer in ventilated rooms to be performed efficiently.

Keywords: Indoor airflow, Thermal wall jets, Heat transfer, Large-Eddy Simulation, Lattice-Boltzmann Method

1. Introduction

Heating, ventilation, and air conditioning (HVAC) systems are widely used in buildings, ensuring occupants' thermal comfort and maintaining acceptable indoor air quality. This is achieved through the management of air properties, including temperature, humidity, cleanliness, and distribution, in accordance with the specific needs of the conditioned space. However, HVAC systems are the most consuming end-use worldwide, accounting for 38 % of

buildings consumption [1]. Consequently, it is of great importance to design energy-efficient HVAC systems and to optimize their integration into buildings. To this end, it is necessary to have a comprehensive understanding of the indoor airflow dynamics induced by these systems. This task is particularly complex due to the large-scale building geometries, interactions with walls, thermal effects, and the coexistence of diverse flow regimes, spanning from laminar to turbulent, under transient conditions.

Experimental investigations can provide detailed information on flow characteristics at specific locations in the area of interest. However, they are often costly, time-consuming, and logistically difficult to implement. As an alternative, CFD-based simulations have been widely adopted, as they provide detailed data at every point within the flow domain, enabling the investigation of complex flow structures - information that is useful for designing thermally comfortable, healthy, and energy-efficient buildings. Nonetheless, performing CFD studies necessitates careful attention to model selection, incorporating physical, mathematical, and numerical assumptions tailored to the specific flow characteristics, and precise simulation setup to obtain accurate predictions.

Two predominant CFD approaches have received considerable attention in the field of building simulation: Reynolds-averaged Navier-Stokes simulations (RANS) and Large-Eddy Simulation (LES). RANS methods are based on the assumption that turbulence is a statistical process characterized only by the temporal distribution at each computational point, thereby modeling

all eddies. In contrast, LES is based on the separation of large and small turbulent scales, and the most energy-carrying and problem dependent eddies are explicitly resolved, while the smallest vortices are modeled. Over the past two decades, the numerous studies documented in the scientific literature have more frequently used RANS approaches than LES [2]. This can be explained in part by the ability of RANS simulations to adequately characterize mean parameters in fully turbulent airflows with reasonable computational resources [3, 4]. However, LES has the potential to provide more accurate and reliable results than RANS simulations. Indeed, LES stands out when it comes to turbulent flows that are not fully developed, transient or anisotropic, for which it gives a more complete description [5]. Nevertheless, LES does not yet benefit from guidelines as well established as those for RANS approaches [6, 7, 8]. Moreover, LES implies greater computational complexity and a significant increase in computational costs, which prevents its application for large-scale geometries.

Table 1 gives a non-exhaustive overview of LES simulations applied to mechanically ventilated rooms. These simulations predominantly involve canonical jets that develop within experimental configurations sourced from references such as Nielsen et al. [9], Blay et al. [10], and Posner et al. [11]. The Reynolds numbers of the studied flows are generally within the low range $Re \leq 5000$ at the ventilation outlet. Several of these investigations have specifically aimed to incorporate thermal phenomena into LES studies, introducing varying degrees of buoyancy influence, typically represented by

Table 1: Example of existing LES simulations applied to mechanically ventilated rooms.

Authors	**Configuration**	**Airflow type**	$\boldsymbol{Re}$	**Thermal ($\boldsymbol{Ar}$)**	**Subgrid-scale models**	**Mesh size**	$\boldsymbol{R = \frac{t_{wc}}{t_{phy}}}$
Sakamoto and Matsuo [18]	$2 \times 2 \times 2$ m room	vertical square jet	-	no	Deardoff	5.83×10^3	-
Davidson [19]	$W/H = 1$, $L/H = 3$ room (from Nielsen et al. [9])	horizontal planar jet	5000	no	DS, Dynamic one-equation	3.93×10^5	-
Zhang and Chen [20]	$W/H = 1$, $L/H = 3$ room (from Nielsen et al. [9])	horizontal planar jet	5000	no	SS, filtered DS	2.36×10^4	-
	$1.04 \times 1.04 \times 0.7$ m heated room (from Blay et al. [10])	horizontal planar jet	678	yes (0.0036)		4.61×10^4	-
Su and Chiang [21]	$W/H = 1$, $L/H = 3$ room (from Nielsen et al. [9])	horizontal planar jet	5000	no	SS, filtered DS,	7.63×10^4	-
	$5.16 \times 3.65 \times 2.43$ m rooms with occupants and objects	horizontal square jet	-	yes (-)	Stimulated small-scale	1.03×10^5	360 (1 core)
Kuznik et al. [17]	$3.1 \times 3.1 \times 2.5$ m room (from Kuznik [22])	horizontal round jet	12000	yes ($0.02/-0.012$)	RNG	1.60×10^6	1500 (1 core)
Tian et al. [23]	$0.914 \times 0.457 \times 0.305$ m partitioned room (from Posner et al. [11])	vertical square jet	1500	no	RNG	3.97×10^5	-
Wang and Chen [14]	$2.44 \times 2.44 \times 2.44$ m room with a heated box	horizontal planar jet	2600	yes (-)	DS, WALE, Dynamic kinetic energy	3.73×10^5	-
Abdilghanie et al. [15]	$2.44 \times 1.83 \times 2.44$ m room	vertical square jet	4895	no	SS, DS	2.95×10^5	160 (20 cores)
Kempe and Hantsch [24]	$2.44 \times 2.44 \times 2.44$ m room with a heated box	horizontal planar jet	2600	yes (-)	Sigma	2.10×10^6	46 (8 cores)
Morozova et al. [16]	$1.04 \times 1.04 \times 0.7$ m heated room (from Blay et al. [10])	horizontal planar jet	684	yes (0.191)	WALE, S3PQ	1.15×10^6	5000 (1 core)
Auvinen et al. [25]	170 m^3 real restaurant room	horizontal square jets	-	no	modified two-part SS	283×10^6	44 (864 cores)

scenario.

A promising alternative to conventional CFD approaches based on the Navier-Stokes equations is the Lattice Boltzmann Method (LBM), which is very efficient to perform LES simulations of low Mach number separated flows [26]. Indeed, the LBM computation process remains entirely local, where computations at each node only require data acquired from that node or its nearest neighbors. Also, the LBM does not involve the Poisson equation to link pressure and velocity fields in the context of incompressible flows, which can be difficult to solve due to its non-locality. These inherent characteristics make the LBM method well suited to high performance computing on parallel architectures. In addition, mesh generation is facilitated through the use of embedded uniform meshes with a fixed grid step ratio of two between successive refinement levels. The incorporation of immersed boundary conditions further simplifies the handling of complex geometries, such as rooms and buildings. However, LBM-based LES applications in building simulation have only recently begun to emerge, with only few studies on mechanically ventilated rooms. Elhadidi and Khalifa [27] carried out one of the earliest investigations, comparing coarse grid LBM-LES with RANS simulations based on a finite volume (FV) framework for real-time simulation. The results of the study showed that both models successfully predicted the correct flow patterns and temperature field, but the FV-RANS approach was both faster and more time accurate than the LBM for unsteady simulations on coarse grids. Subsequent studies, including those by Khan et al. [28], Han et al.

[29], have followed the same line of research and come to similar conclusions. Sajjadi et al. [30] compared LBM-LES and LBM-RANS simulations of indoor airflow and concluded that LBM-LES predictions outperformed LBM-RANS predictions in terms of accuracy, but at the cost of higher computational demand. Jahidul Haque et al. [31] assessed the effects of various subgrid scale models on LBM-LES simulations, particularly in the context of inhomogeneous turbulent airflow patterns within a model room with partitions, and found that there are significant differences in the results due to different subgrid scale models. Han et al. [32] were the first to introduce near-wall modeling in LBM-LES to study flows in the built environment, resulting in improved simulation accuracy even when using coarser grids, thus reducing computational requirements. Siodlaczek et al. [33] performed LBM-LES to evaluate airflow around a seated thermal manikin, highlighting the interest of LBM-LES in the study of thermal comfort, particularly in the context of indoor environmental analysis. Hu et al. [34] applied a framework combining LBM, LES, and Markov chains to simulate unsteady particle transport in indoor environments, and found it to be faster than FV-based models while maintaining accuracy. Bazdidi-Tehrani and Sargazizadeh [35] discusses the use of a parallel LBM-LES solver to simulate particle flow in a single ventilated model room, demonstrating good prediction accuracy and significantly reduced computational time compared to FV-LES.

Despite these efforts to demonstrate the feasibility of LBM-LES for indoor airflow applications, it is worth noting that, to the best of our knowledge, no

comprehensive validation studies that compare LBM-LES predictions with experimental measurements of thermal indoor airflow under realistic configurations exist in the literature. Consequently, the aim of this contribution is to evaluate the predictive capacity of an LBM-LES approach, developed within the ProLB framework [36], for the prediction of thermal jet flows developing in a mechanically ventilated room. In particular, this study focuses on three cases, an isothermal jet, a hot jet, and a cold jet, generated by an air diffuser of complex design, and developing near the ceiling of the full-scale MINIBAT test room. This configuration was studied experimentally by Kuznik [22], whose research objective was to provide detailed experimental data to make recommendations on the use of CFD to model a technical building ventilation systems. This has led to several papers on the physical analysis of airflow [37] and CFD modeling based on RANS approaches [38, 39, 40, 41] and LES [17]. The present study extends this to LBM-LES and validates the simulations by extensive comparisons with a comprehensive experimental dataset on mean velocity and temperature profiles as well as turbulent quantities.

The paper is organized as follows. Section 2 presents the MINIBAT test room and outlines the experimental conditions. Section 3 focuses on numerical modeling, including modeling methods and a grid sensitivity study. Section 4 discusses the simulation results with respect to the experimental data and analyses the jet structure of the cases studied. Lastly, Section 5 gives concluding remarks.

2. Experimental setup

2.1. The Minibat test room

Figure 1 shows the experimental full-scale MINIBAT test room. The configuration is an enclosure with spatial dimensions of 3.10 m in the x-direction, 3.10 m in the y-direction, and 2.50 m in the z-direction.

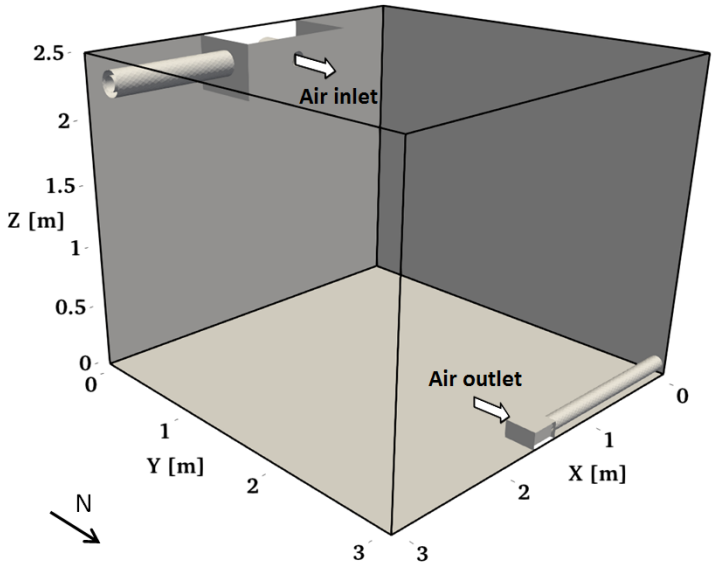

Figure 1: Illustration of the MINIBAT experimental test room and its dimensions. The direction is indicated to locate the different walls.

A thermal guard regulates the air temperature around the room at a constant temperature of 21.5 °C. The southern facade of the room consists of a glazed wall, while the remaining vertical walls are made of oriented strand board covered on the inside with plasterboard. The internal surface of the ceiling is made of plasterboard fixed to a plywood panel insulated with glass wool. The floor is a cellular concrete slab. Detailed information on the

physical properties and thicknesses of the walls can be found in Kuznik [22].

An axisymmetric jet is generated within the room by a home-designed ventilation system shown in Figure 2a. This air supply system is positioned at the top of the south wall (Figure 1), and its design is tailored to achieve the desired axisymmetric structure of the jet. Specifically, the air inlet, characterized by a diameter D of 0.12 m, is positioned at an offset of 0.57 m from the south wall and 0.18 m from the ceiling. Air extraction, shown in Figure 2b, is facilitated by an exhaust vent located in the lower part of the wall opposite the ventilation system (Figure 1). The entire ventilation and exhaust system operates in a closed circuit and is thermally insulated to maintain controlled conditions.

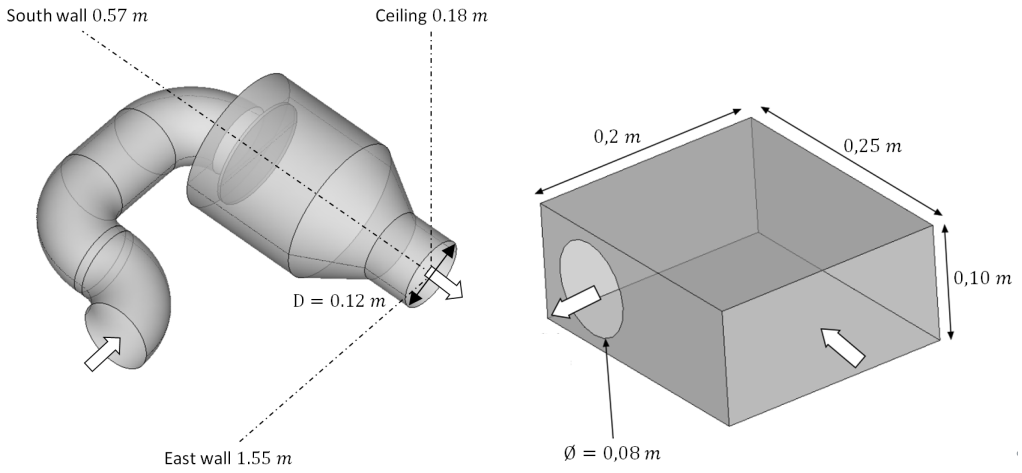

(a) Air supply (b) Air exhaust

Figure 2: Schemes of the air inlet and outlet devices, their dimensions, and distances from walls.

2.2. Metrology

The inlet and outlet flow rates controlled by the ventilation system were measured using two flow-meters with an accuracy of $\pm 0.5\,\mathrm{m^3\,h^{-1}}$. Inside the room, the air temperature was measured using three Pt100 sensors with an accuracy of $\pm 0.2\,^{\circ}\mathrm{C}$. Additionally, a three-dimensional hot-wire probe was used to measure all three components of instantaneous velocity, with an uncertainty on the mean velocity measurement of $\pm 0.05\,\mathrm{m\,s^{-1}}$. This probe was calibrated in-situ to facilitate the acquisition of high frequency (5000 Hz) three-dimensional instantaneous velocity data, allowing detailed investigation of flow turbulence. Surface temperature measurement involved the installation of nine thermocouples positioned on each wall with an accuracy of $\pm 0.4\,^{\circ}\mathrm{C}$. A mobile arm was used to move the temperature and air velocity sensors in the room to obtain mean temperature and mean velocity fields.

2.3. Experimental conditions

The experiment was carried out under steady-state conditions, and the characteristics of the three cases studied, namely an isothermal jet, a hot jet, and a cold jet, are presented in Table 2. In this table, T_{in} and U_{in} represent the temperature and velocity respectively at the inlet of the ventilation system. Ar_D and Re_D are the Archimedes number ($Ar_D = g\beta(T_{in} - T_{ref})D/U_{in}^2$) and the Reynolds number ($Re_D = U_{in}D/\nu$), respectively, with respect to the blowhole diameter D. T_{ref} is a reference temperature corresponding here to the mean air temperature of the non-moving fluid zone, g is the gravity,

Table 2: Experimental conditions for the jets studied.

Case	T_{in} [°C]	Ar_D [–]	Re_D [–]	U_{in} [$\mathrm{m\,s^{-1}}$]
Isothermal	21.8	0.0	23680	2.96
Hot	30.9	0.0028	21600	2.70
Cold	12.7	−0.014	11720	1.47

Table 3: Mean surface temperature in °C.

Case	South	North	East	West	Floor	Ceiling
Isothermal	21.8	21.7	21.7	21.7	21.8	21.7
Hot	24.3	25.0	24.6	24.7	24.5	25.5
Cold	22.6	20.8	21.0	21.0	20.7	21.0

ν is the kinematic viscosity, and β is the coefficient of thermal expansion. The Archimedes number characterizes the initial buoyancy force relative to the initial inertial force. The corresponding experimental data can be downloaded from Gresse et al. [42].

Table 3 provides the average temperature values for each surface within the room, based the nine thermocouples positioned on each wall.

2.4. Description of the jet flows

Figure 3 shows the experimental mean velocity vector fields in the symmetry plane of the jet, corresponding to the median plane of the room at $x = 1.55\,\mathrm{m}$. For the sake of clarity, only a limited subset of vectors is shown in the figure. The coordinates within the figure have been scaled with respect to the diameter D of the blowhole and the distance H from the center of the

202 blowhole to the ceiling.

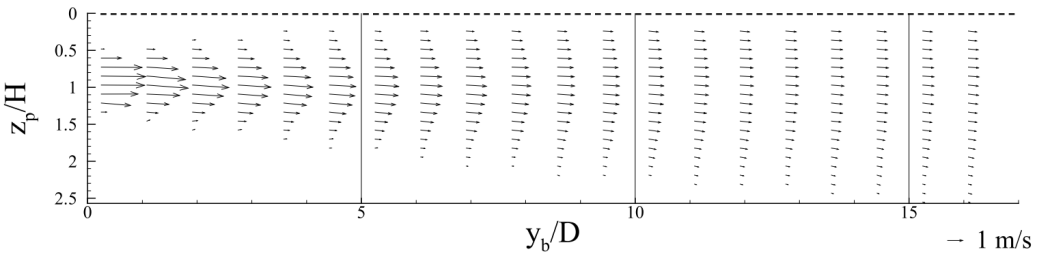

(a) Isothermal jet

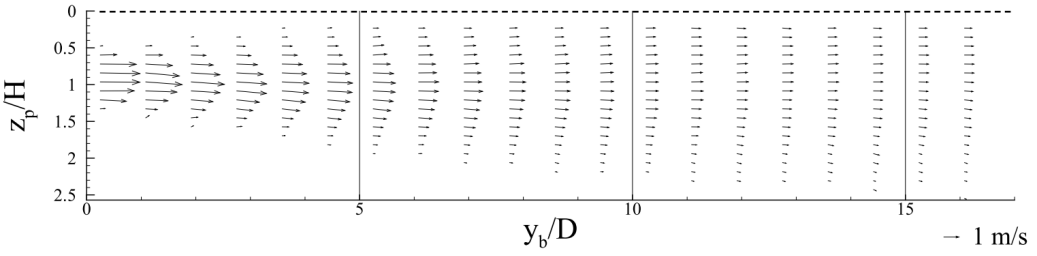

(b) Hot jet

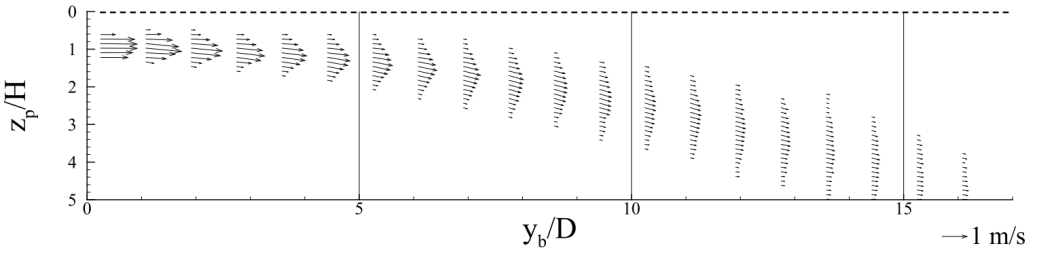

(c) Cold jet

Figure 3: Experimental mean velocity vector fields in the symmetry plane of the jet, corresponding to the median plane of the room at $x = 1.55\,\mathrm{m}$ (from Kuznik [22]).The coordinates have been scaled with respect to the diameter D of the blowhole, and the distance H from the center of the blowhole to the ceiling.

203 Both the isothermal jet and the hot jet exhibit a characteristic behavior of
204 adhering to the ceiling, resulting from the expansion of the axisymmetric jet.
205 Additionally, the hot jet is influenced by buoyancy, with the effect increasing
206 with distance from the air inlet. However, as the Archimedes number is small,

the buoyancy effect remains relatively weak. The cold jet behaves differently to the other two cases. It falls without interacting with the ceiling due to a significant buoyancy effect, characterized by a negative Archimedes number five times greater in absolute value than that of the hot jet.

3. Numerical Modeling

3.1. The thermal LBM-LES framework

The LBM is used to simulate the macroscopic behavior of fluids. However, unlike conventional solvers, which are based on a macroscopic approach by directly solving the Navier-Stokes equations, the LBM is derived from the kinetic theory and the Boltzmann equation based on a mesoscopic description of the flow [26].

The fluid dynamics is simulated through streaming and collision steps based on the lattice Boltzmann equation:

$$f_\alpha(\vec{x} + \vec{c_\alpha}\Delta t, t + \Delta t) - f_\alpha(\vec{x}, t) = \Omega_\alpha(\vec{x}, t) \tag{1}$$

where $\vec{x}$ is the physical space vector, t is the time, Δt is the time step, $\vec{c_\alpha}$ is a set of discrete velocities with the subscript $_\alpha$ indicating the discrete velocity direction, usually a D3Q19 for three-dimensional problems (3 space dimensions, 19 discrete velocities), $f_\alpha(\vec{x}, t)$ is the discrete distribution function, and $\Omega_\alpha(\vec{x}, t)$ is the collision operator representing a source term responsible for the redistribution of f_α due to inter-particle collisions.

The expression of the collision operator can be simplified using the Bhatnagar-Gross-Krook (BGK) operator [43] (Equation 2), which corresponds to the relaxation of the distribution function f_α towards the equilibrium Maxwell-Boltzmann distribution function f_α^{eq}, with the relaxation time parameter τ.

$$\Omega_\alpha(\vec{x}, t) = -\frac{1}{\tau}(f_\alpha - f_\alpha^{eq}) \tag{2}$$

The equilibrium distribution function f_α^{eq} is given by:

$$f_\alpha^{eq} = \omega_\alpha \rho \left(1 + \frac{c_{\alpha,i} u_i}{c_s^2} + \frac{u_i u_j (c_{\alpha,i} c_{\beta,i} - c_s^2 \delta_{ij})}{2 c_s^4}\right) \tag{3}$$

with ω_α the weighting coefficients of the D3Q19 scheme, ρ is the mass density, u_i is the macroscopic velocity, and $c_s = \frac{1}{\sqrt{3}}$ the pseudo speed of sound.

In the current model, some adjustments have been made to the collision operator to enhance computational stability while maintaining the simplicity and accuracy of the approach. In particular, these adjustments include the addition of a third-order expansion for the equilibrium function and the implementation of a hybrid recursive reconstruction procedure [44].

Macroscopic variables, such as the density ρ and the flow momentum $\rho\vec{u}$, can be derived from the moments of the distribution functions f_α using the following expressions:

$$\rho = \sum_{\alpha} f_{\alpha} \tag{4a}$$

$$\rho \vec{u} = \sum_{\alpha} \vec{c_{\alpha}} f_{\alpha} \tag{4b}$$

The application of the Chapman-Enskog theory for small Knudsen numbers allows for the derivation of the second-order weakly compressible 3D Navier–Stokes equations. This procedure establishes a fundamental relationship (Equation 5) that relates the relaxation time τ to the kinematic viscosity ν, and it incorporates the pseudo speed of sound c_s.

$$\nu = c_s^2 \left(\tau - \frac{\Delta t}{2} \right) \tag{5}$$

To take into account source terms S, the right-hand side of Equation 1 can be modified as follows:

$$f_{\alpha}(\vec{x} + \vec{c_{\alpha}} \Delta t, t + \Delta t) - f_{\alpha}(\vec{x}, t) = \Omega_{\alpha}(\vec{x}, t) + S_{\alpha}(\vec{x}, t) \tag{6}$$

The method used to integrate an external force F into the LBM framework is based on the approach introduced by Guo et al. [45]. In particular, the following development can be considered to accurately recover the Navier–Stokes equations:

$$S_{\alpha} = \left(1 - \frac{\Delta t}{2\tau} \right) F_{\alpha} = \left(1 - \frac{\Delta t}{2\tau} \right) \omega_{\alpha} \left(\frac{c_{\alpha,i}}{c_s^2} + \frac{(c_{\alpha,i} c_{\beta,i} - c_s^2 \delta_{ij}) u_j}{c_s^4} \right) \vec{F} \tag{7}$$

A term is also added in the expression of macroscopic moments:

$$\rho = \sum_{\alpha} f_{\alpha} + \frac{\Delta t}{2} \sum_{\alpha} F_{\alpha} \tag{8a}$$

$$\rho \vec{u} = \sum_{\alpha} \vec{c_{\alpha}} f_{\alpha} + \frac{\Delta t}{2} \sum_{\alpha} \vec{c_{\alpha}} F_{\alpha} \tag{8b}$$

In the present study, since the temperature variations are moderate, the buoyancy effect is accounted for by the Boussinesq source term in the discretized Boltzmann equation:

$$\vec{F} = -\vec{g}\beta(T - T_{ref}) \tag{9}$$

The incorporation of an external force to simulate buoyant airflows under the Boussinesq approximation in the current LBM framework has already been validated on well-established benchmark problems such as a double diffusive Rayleigh-Bénard convection or a 2D and 3D thermal rising bubble, as presented in Feng et al. [46].

Thermal calculations are addressed through a hybrid approach [47]: the velocity field is solved using the LBM, while the energy equation is calculated independently using a classical finite volume method. Compared to the multi-speed approach [48] or the double-population approach [49], the hybrid approach is more stable, minimizes the number of degrees of freedom of the global method, and reduces the memory requirements. Specifically, the temperature advection-diffusion equation is solved using the second-order Mono-

tonic Upstream-centered Scheme for Conservation Laws (MUSCL), while the conventional second-order centered-difference scheme is applied to the diffusion and viscous dissipation terms.

Finally, the Vreman subgrid-scale model [50] is integrated into the LBM framework to perform LES. This particular model demonstrates strong performance in fully developed turbulent shear flows, transient flows, and the near-wall region without the need for a dynamical procedure, as discussed in Jacob et al. [44]. It has also been successfully applied in the context of building applications, as highlighted in Jahidul Haque et al. [31], but without considering thermal effects.

3.2. Numerical settings

3.2.1. Boundary conditions

The numerical problem requires the specification of three types of boundary conditions: air inlet conditions, air outlet conditions, and wall boundary conditions.

Kuznik and Brau [38] have demonstrated that, in the context of real ventilation, the pressure field at the inlet is the main parameter determining the structure of the developing jets in the room. The direct imposition of inlet boundary conditions at the blowhole requires a detailed understanding of the flow at this location. However, obtaining such information is often challenging and computationally complex to implement. Consequently, the experimental air supply duct is explicitly modeled and the inlet conditions

are imposed far from the inlet diffuser, at a fully developed flow section. The velocity and temperature values are set according to the experimental data given in Table 2. Similarly, the experimental air outlet duct is explicitly modeled and the outlet boundary conditions are imposed at a fully developed flow section. A constant density is applied and the velocity and temperature gradients normal to flow direction are set to zero.

At wall surfaces, classical no-slip boundary conditions for velocity are enforced, along with fixed temperature values derived from the measurements presented in Table 3. To avoid the need to use an excessively fine mesh at walls to fully resolve the boundary layer, wall functions are used to calculate the temperature and velocity values at the first fluid nodes. The LBM-LES solver used here is based on an immersed boundary approach to handle arbitrary geometries while using an embedded Cartesian grid. Details on the implementation of the boundary conditions, including the coupling with wall models for turbulent flows, can be found in Wilhelm et al. [51]. Specifically, the velocity wall function developed by Afzal [52], which accounts for curvature and adverse pressure gradient effects, is used in the air supply section. The explicit velocity wall function of Cai and Sagaut [53] and the temperature wall function of Kader [54] are applied at the wall surfaces. It is noteworthy that the Kader's temperature wall function was originally designed for fully turbulent flows and may underestimate convective heat transfer at walls in cases of mixed or natural convection [55]. To address this limitation, the wall turbulent Prandtl number $Pr_{t,w}$ of the temperature wall function

is adjusted. Since $Pr_{t,w}$ compares the momentum eddy diffusivity to the heat transfer eddy diffusivity, its value should be lower in natural or mixed convection scenarios compared to forced convection (typically $Pr_{t,w} = 0.85$). Previous work by Zhang et al. [56] adjusted $Pr_{t,w}$ to obtain convective heat transfer coefficients on walls consistent with correlation formulas. In this study, the $Pr_{t,w}$ values were adjusted to $Pr_{t,w} = 0.025$ on all walls for both the hot and cold jets, close to the values obtained in Zhang et al. [56]. For the hot jet, the value on the ceiling was adjusted to $Pr_{t,w} = 0.2$, due to the interaction of the jet with the ceiling resulting in a mixed convection airflow.

3.2.2. Computational mesh

The computational domain is discretized into a series of nested volumes of uniform Cartesian grid cells. The mesh is refined in the air supply duct with a mesh size of $\Delta x = D/35$. This mesh size ensures the presence of at least 8 grid points in the narrowest regions of the air supply duct. The jet development zone and the exhaust duct are discretized with a mesh size of $\Delta x = D/17.5$ and the rest of the domain is discretized with a mesh size of $\Delta x = D/2.1875$. Transitional zones with mesh sizes of $\Delta x = D/8.75$ and $\Delta x = D/4.375$ are automatically introduced between the jet development zone and the rest of the domain, and between the exhaust vent and the rest of the domain. In total, 4.9×10^6 grid points are used to mesh the entire domain. The resulting computational time steps are $3.37 \cdot 10^{-5}$ s for the isothermal and hot simulations, and $6.74 \cdot 10^{-5}$ s for the cold jet simulation.

These time steps were used to limit the maximum Mach number to 0.075 and to ensure compliance with the low Mach condition of the LBM. With this mesh resolution, the parallel computations were performed on 288 Intel Skylake processors @ 2.7GHz, 2x24 cores (AVX 512). The resulting total computational cost for one case is about $8.0 \cdot 10^4$ CPU hours with a ratio R (t_{wc}/t_{phy}) of $1.85 \cdot 10^3$.

To ensure the validity of the averaged results presented below, the statistical convergence of the simulations was first verified. After obtaining steady-state conditions, the statistics are computed at $15T^*$, where $T^* = L_c/U_c$ denotes the convective time derived from the characteristic parameters with $L_c = 4.65\,\mathrm{m}$ and $U_c = 2\,\mathrm{m\,s^{-1}}$ for the hot jet, and $U_c = 1\,\mathrm{m\,s^{-1}}$ for the cold jet.

3.3. Grid sensitivity study

To analyze the influence of the grid on the results, the *medium* mesh previously defined was tested together with a $coarse$ and a $fine$ mesh with different refinements in the jet development zone, as reported in Table 4. Figures 4 and 5 show the mean velocity magnitude and turbulence intensity profiles at different positions along the y-axis in the symmetry plane of the jet. These profiles have been derived from simulations of the isothermal jet for the three meshes considered. Turbulence intensity is defined as the root mean square of the velocity fluctuations normalized by the maximum mean velocity, as expressed in Equation 10. Its formulation is directly related to

Table 4: Parameters for the grid sensitivity study.

Grid	Δx in the jet development zone (m)	Grid points (10^6)
$coarse$	D/8.75	1.5
$medium$	D/17.5	4.9
$fine$	D/35	31.2

the diagonal components of the Reynolds stress tensor R_{ij}.

$$I_t = \frac{\sqrt{\frac{1}{3}(\overline{u_x'^2} + \overline{u_y'^2} + \overline{u_z'^2})}}{U_{max}} \tag{10}$$

The results from the $medium$ and $fine$ meshes for both the mean velocity and turbulence intensity profiles are very similar across all y-positions. The discrepancies remain below $0.2\,\mathrm{m\,s^{-1}}$ for the mean velocity and below 3 % for the turbulence intensity. In contrast, the results from the $coarse$ mesh show noticeable deviations, mainly due to excessive numerical diffusion. Compared to the $medium$ mesh, the velocity maximum shows a position shift with increasing z between $y = 0.9\,\mathrm{m}$ and $y = 1.5\,\mathrm{m}$, and an underestimation of its value up to $0.45\,\mathrm{m\,s^{-1}}$. For turbulence intensity, a similar conclusion can be drawn with an underestimation up to 10 %. The $medium$ mesh, therefore, proves to be a good compromise between accuracy and computational cost in the case studied. Nevertheless, the subsequent analysis of the jet will be based on calculations performed with the $fine$ mesh shown in Figure 6 in the median plane of the room, given its availability. It should be noted that the conclusions are still valid for the other two thermal cases.

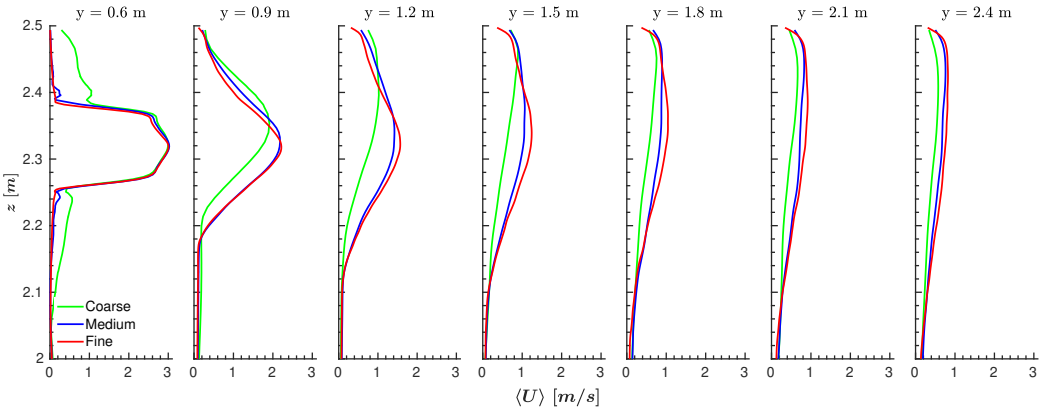

Figure 4: Mean velocity profiles at different positions along the y-axis in the symmetry plane of the jet for the isothermal case obtained with the three different meshes.

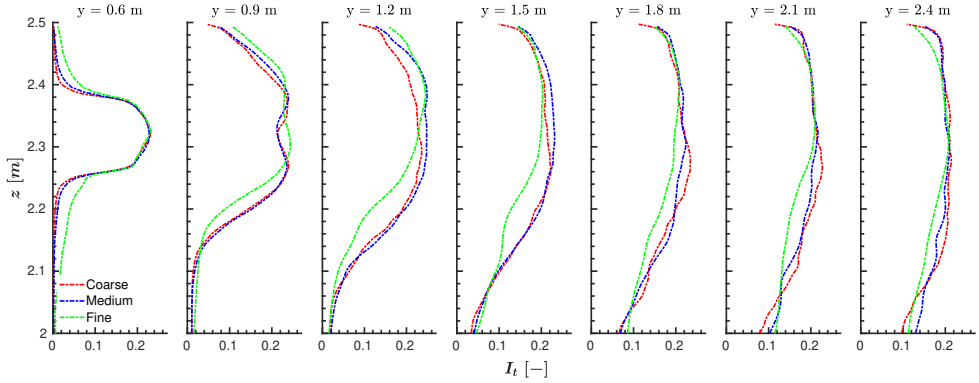

Figure 5: Turbulence intensity profiles at different positions along the y-axis in the symmetry plane of the jet for the isothermal case obtained with the three different meshes.

4. Validation

This section provides a comprehensive comparative analysis between the experimental data and the current simulation results. The airflow analysis focuses on the mean profiles of velocity, temperature, and turbulence intensity in the symmetry plane of the jet. The jet axis is indicated by dotted lines on the plots. In addition, the turbulence distribution is evaluated using

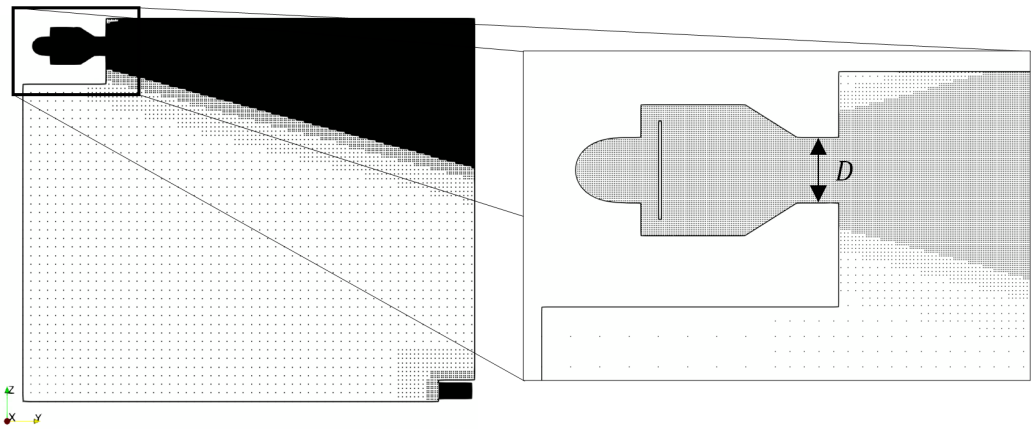

Figure 6: Representation of the *fine* mesh in the median plan of the room, with a zoomed-in view of the air supply area.

the Lumley triangles as defined in the corresponding section. Finally, the jet structures obtained are presented and analyzed.

4.1. Mean Velocity Profiles

Figure 7 shows the experimental and simulated mean velocity profiles in the symmetry plane of the jet for the isothermal, hot, and cold cases. For the isothermal and hot jets adhering to the wall (Figures 7a and 7b), the shapes of the simulated profiles are in good agreement with the experimental profiles. Small discrepancies are observed in the region near the ceiling ($2.32\,\mathrm{m} \leq z < 2.5\,\mathrm{m}$), where the velocity is overestimated up to $0.2\,\mathrm{m\,s^{-1}}$ for the isothermal jet and $0.4\,\mathrm{m\,s^{-1}}$ for the hot jet. This discrepancy can be attributed to the possible underestimation of the shear rate by the wall model, despite its adjustment, as well as to the influence of buoyancy modeling, which tends to accentuate the rise of the jet towards the ceiling from $y = 1.2\,\mathrm{m}$. However, the experimental velocity measurements near the ceiling were made with a hot-

wire probe. This introduces complexities associated with radiative exchange with the wall, which could lead to unaccounted errors in the measurements. In contrast, the cold jet (Figure 7c) falls due to buoyancy, preventing any interaction with the ceiling. The shapes of the simulated profiles are in good agreement with the experimental data. The velocity maxima are accurately predicted by the simulation, with only a small position shift of less than 0.1 m with increasing z from $y = 1.5\,\mathrm{m}$, and a slight overestimation of the vertical expansion. Despite these minor discrepancies, the simulation adequately captures the dynamics of the three jets studied.

4.2. Mean Temperature Profiles

Figure 8 shows the experimental and simulated mean temperature profiles in the symmetry plane of the jet for the two thermal cases. A remarkable accuracy is observed in the prediction of temperature values in the central region of the room. For example, the temperature at the center of the room is accurately predicted to be 25.8 °C for the hot jet and20.6 °C for the cold jet. This accuracy is due to the adjustment of the near-wall modeling, in particular the adjustment of $Pr_{t,w}$, which effectively accounts for convective heat transfer at the room walls. Regarding the temperature profiles within the jet, those of the hot jet (Figure 8a) are in very good agreement with the experimental data, but they differ more for the cold jet (Figure 8b). Indeed, while the temperature maxima on the various profiles are accurately estimated, small position shifts of about 0.1 m are observed with increasing z,

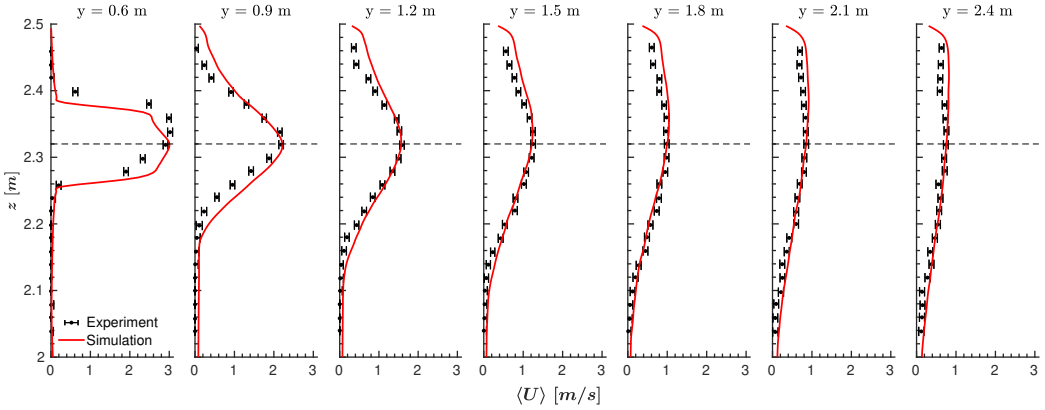

(a) Isothermal jet

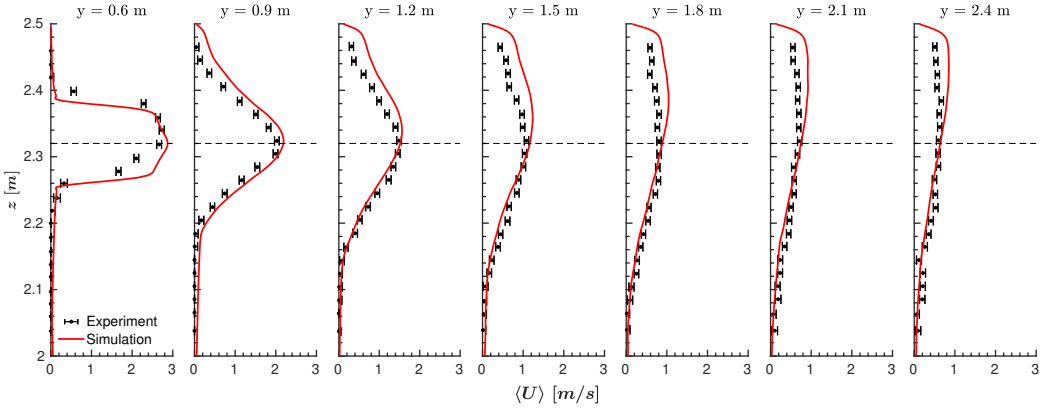

(b) Hot jet

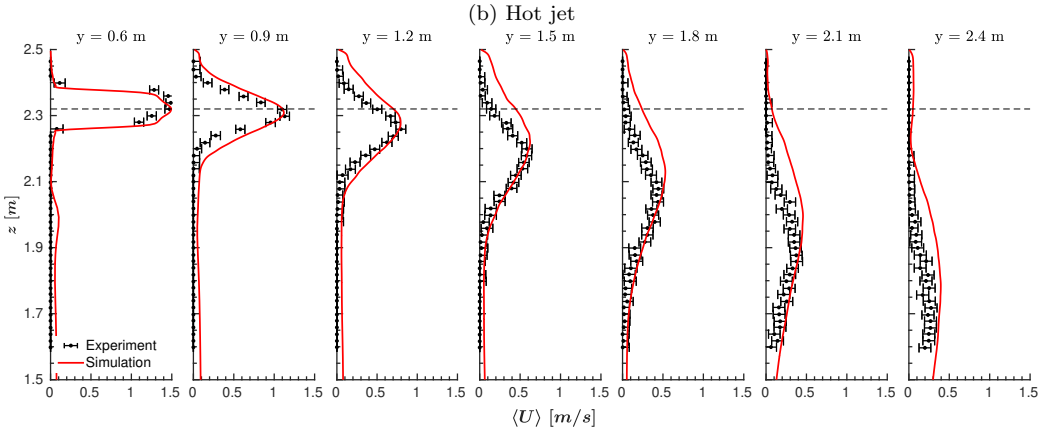

(c) Cold jet

Figure 7: Mean velocity profiles at different positions along the y-axis in the symmetry plane of the jet for the three cases.

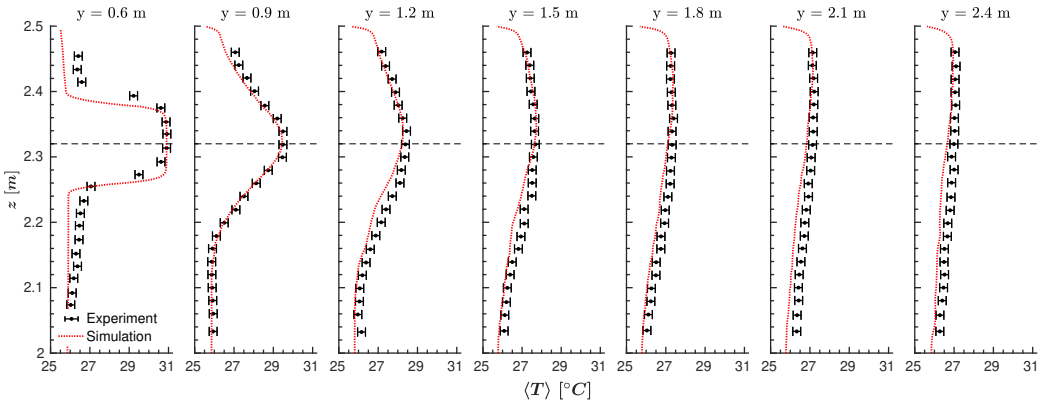

(a) Hot jet

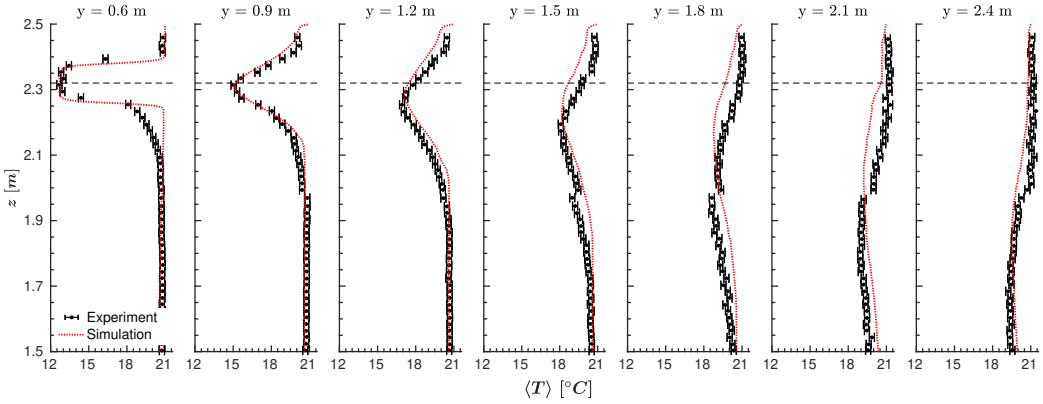

(b) Cold jet

Figure 8: Mean temperature profiles at different positions along the y-axis in the symmetry plane of the jet for the two thermal cases.

especially at $y = 1.8\,\mathrm{m}$ and $y = 2.1\,\mathrm{m}$. These shifts are comparable to those observed in the mean velocity profiles. Despite these minor discrepancies, the adopted model efficiently captures turbulent heat transfer mechanisms and buoyancy phenomena within the fluid core and near the wall.

4.3. Mean Turbulence Intensity Profiles

The jet turbulence is first analyzed by examining the turbulence intensity, a parameter of significant relevance due to its potential impact on human

thermal perception [57].

Figure 9 shows the experimental and simulated mean turbulence intensity profiles in the symmetry plane of the jet for the isothermal case, the hot case, and the cold case. The experimental profiles exhibit different characteristics. For the isothermal jet (Figure 9a), the maximum turbulence intensity gradually increases from 20 % near the blowhole to 25 % at $y = 1.2\,\mathrm{m}$, followed by a tendency to stabilize up to $y = 2.4\,\mathrm{m}$. In the case of the hot jet (Figure 9b), the maximum turbulence intensity experiences a more substantial increase, starting from 20 % near the room air inlet, and reaching 32 % at $y = 1.8\,\mathrm{m}$. It then remains relatively stable up to $y = 2.4\,\mathrm{m}$. The maximum turbulence intensity of the cold jet (Figure 9c) exhibits a continuous increase, starting at 20 % near the room air inlet, and reaching nearly 50 % at $y = 2.4\,\mathrm{m}$. The simulation results show good agreement with the experimental profiles for the isothermal jet and the hot jet, but some discrepancies are noted near the room air inlet. In particular, the maximum values are overestimated by 5 % at $y = 0.6\,\mathrm{m}$ and $y = 0.9\,\mathrm{m}$, and tend to be underestimated by less than 10 % beyond $y = 1.5\,\mathrm{m}$ for the hot jet (Figure 9b). On the other hand, the profiles for the cold jet (Figure 9c) deviate more from the experimental data with increasing distance from the room air inlet. The maxima are underestimated by 10 % compared to the measurements, and their positions exhibit a shift of several centimeters with increasing z from $y = 1.8\,\mathrm{m}$. It should be noted that the deviations observed for the cold jet cannot be directly attributed to the mesh refinement. In fact, the grid sensitivity study presented in Sec-

tion 3.3 does not show any noticeable deviations between the *medium* and $fine$ meshes for the turbulence intensity.

4.4. Turbulence anisotropy

Kuznik et al. [37] showed that the interaction, or lack of interaction, between the jets and the ceiling has a significant influence on the evolution of turbulence within the jets, leading to highly anisotropic behaviors. The numerical investigation of Kuznik et al. [39] showed that the use of RANS two equations closure turbulence models is inappropriate because of their inability to predict anisotropy, and suggested that LES could be a solution for the turbulence modeling.

To characterize the turbulence anisotropy, an interpretation of the stress tensor R_{ij} is performed using Lumley triangles. The Lumley triangle [58] provides a graphical representation of the invariants of the Reynolds anisotropy tensor b_{ij}, defined as:

$$b_{ij} = \frac{R_{ij}}{2k} - \frac{1}{3}\delta_{ij} \tag{11}$$

with k the turbulent kinetic energy.

The three principal invariants of the anisotropy tensor, denoted I, II, and III, are computed from the tensor's eigenvalues. Since the first invariant is zero, the Lumley triangle visualizes the map of invariants in the $(-II, III)$ plane, where the left boundary corresponds to axisymmetric contracting turbulence in the form of a disk, the right boundary is associated with axisymmetric expanding turbulence in the form of a cigar, and the top

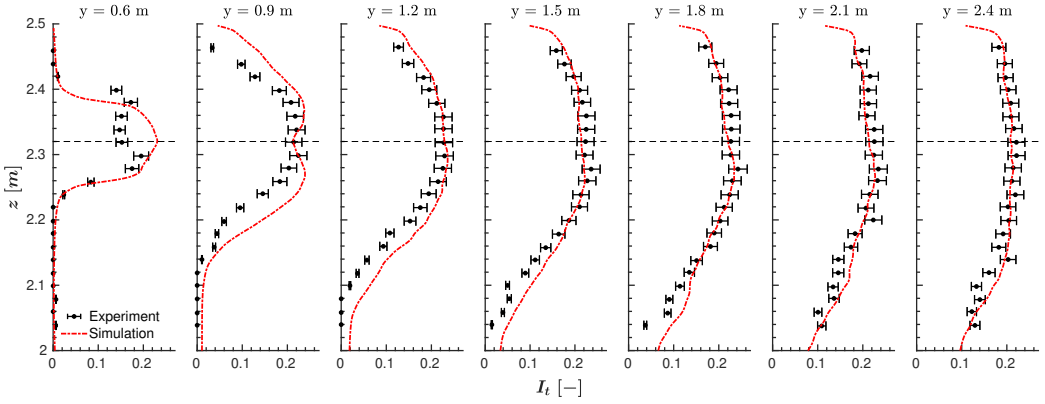

(a) Isothermal jet

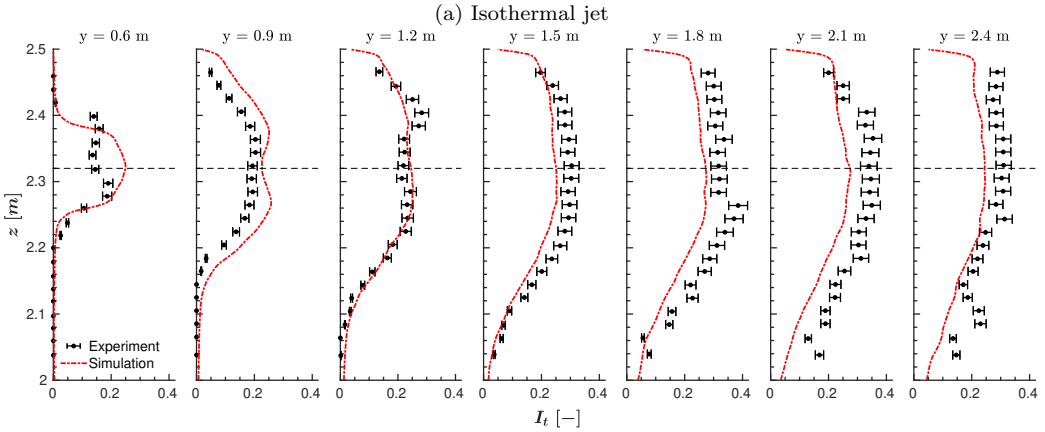

(b) Hot jet

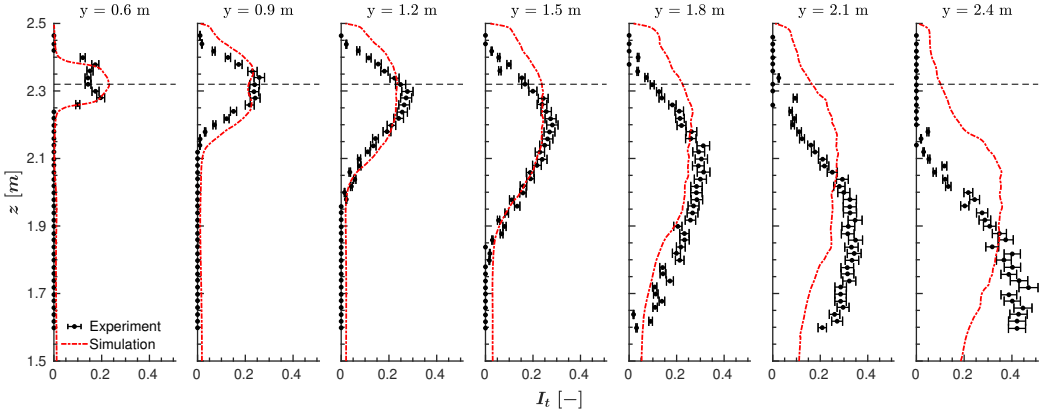

(c) Cold jet

Figure 9: Mean turbulence intensity profiles at different positions along the y-axis in the symmetry plane of the jet for the three cases.

boundary represents a two-dimensional turbulence. In this study, a linearized representation of the invariants ($II*$, $III*$), shown in Figure 10, is used to provide more discriminating characterizations of the turbulence [59].

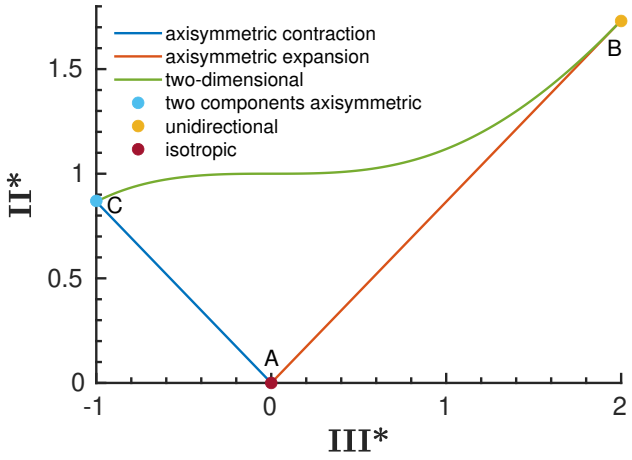

Figure 10: Linearized Lumley triangle representation. The border lines and dots represent the various extreme types of turbulence anisotropy.

Figure 11, 12, and 13 show the experimental and simulated Lumley triangles of measurement points belonging to the the symmetry plane of the jet for the isothermal case, the hot case, and the cold case. In the isothermal case, the turbulence in the experimental jet (Figure 11a) exhibits primarily axisymmetric expansion, tending towards one-dimensional turbulence, with occasional instances of axisymmetric contraction. Kuznik [22] noted that axisymmetric contraction occurs near the blowhole ($y \leq 1.2\,\mathrm{m}$), indicating the presence of coherent ring structures, and that these structures are subsequently distorted by the wall, giving rise to secondary instabilities characterized by longitudinal vortices aligned with the main axis of the jet. The simulation (Figure 11b) captures the main turbulence characteristics of the

experimental jet, characterized by predominantly axisymmetric expansion, with some regions tending towards axisymmetric contraction in the vicinity of the blowhole. In the case of the hot jet (Figure 12a), the experimental Lumley triangle indicates turbulence that is partially axisymmetrically expanding and partially axisymmetrically contracting. Kuznik [22] attributes this behavior to turbulence in the form of lateral ejections superimposed on axisymmetric expansion turbulence. The simulation (Figure 12b) shows slightly more axisymmetrically expanding turbulence than observed in the experiment. For the cold jet (Figure 13a), turbulence is predominantly axisymmetrically expanding, transitioning to a two-dimensional structure, and finally converging to one-dimensional line-like characteristics. Kuznik [22] observed that the two-dimensional structure is confined to the lower part of the jet, while the one-dimensional structure dominates in the upper part. In contrast, the Lumley triangle resulting from the simulation (Figure 13b) shows that the two-dimensional turbulence, which tends to one-dimensional behavior, is less pronounced and gives way to a turbulence pattern with more contraction and axisymmetric expansion, approaching a state of isotropy. Thus, the model used successfully captures the main features of turbulence anisotropy but shows limitations in representing strongly anisotropic phenomena where the turbulence converges to a one-dimensional state.

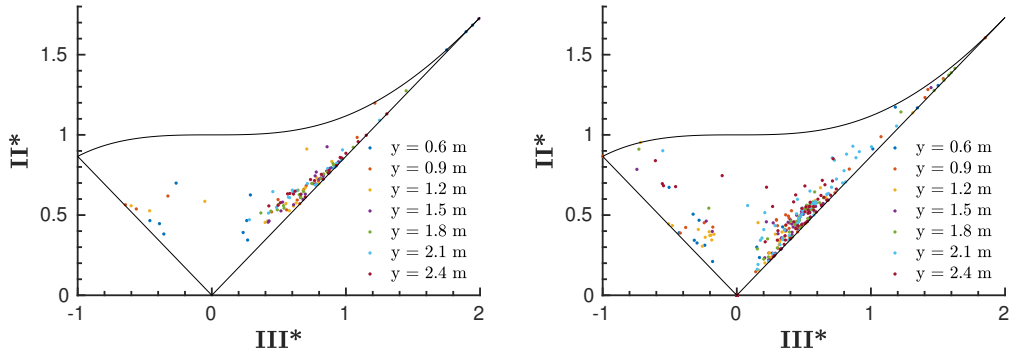

(a) Experimental (b) Simulation

Figure 11: Lumley triangles of measurement points belonging to the symmetry plane of the jet for the isothermal case. The colours of the points correspond to their positions along the y-axis.

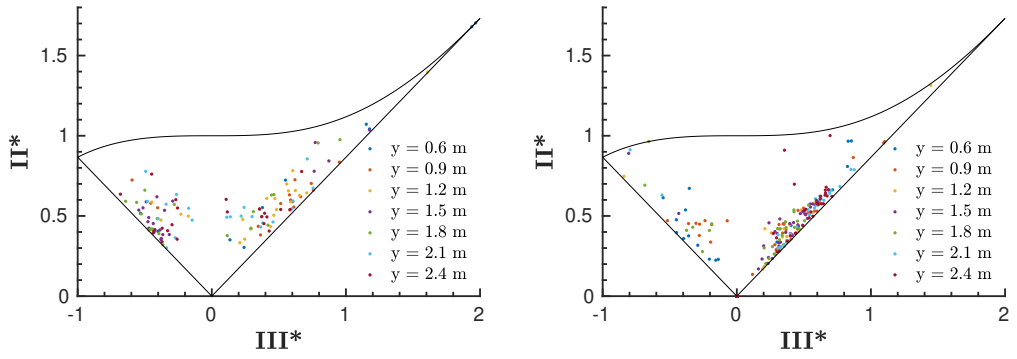

(a) Experimental (b) Simulation

Figure 12: Lumley triangles of measurement points belonging to the symmetry plane of the jet for the hot case. The colours of the points correspond to their positions along the y-axis.

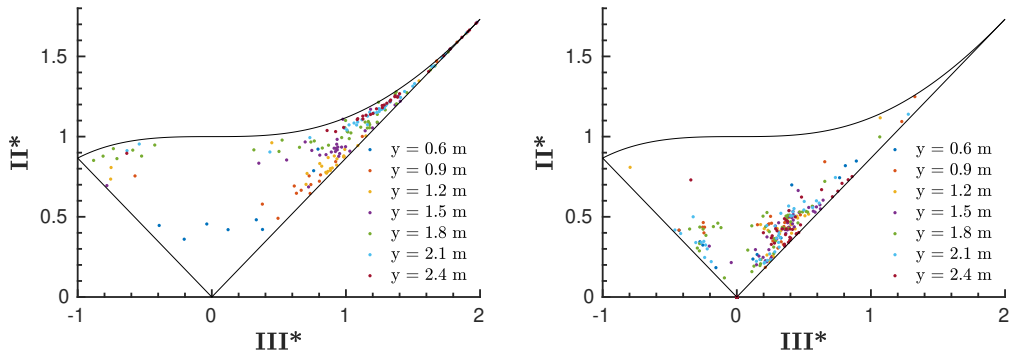

(a) Experimental (b) Simulation

Figure 13: Lumley triangles of measurement points belonging to the symmetry plane of the jet for the cold case. The colours of the points correspond to their positions along the y-axis.

4.5. Jet structures

To illustrate the observations derived from the Lumley triangles, Figure 14 shows isosurfaces of the Q-criterion, defined as the second invariant of the velocity gradient tensor, for the three simulated jets, and colored by normalized vorticity. This three-dimensional visualization effectively highlights the turbulent structures that develop within the jets. In the case of the isothermal jet and the hot jet, their interaction with the ceiling breaks the vortex rings, resulting in their gradual distortion. This process favors the development of vortices primarily aligned with the jet axis. This phenomenon underlies the axisymmetric expansion patterns observed on the Lumley triangles, which are consistent with the experimental results reported by Kuznik [22]. However, the lateral ejection phenomenon described earlier for the hot jet is not evidenced in this visualization. The jets then impact the opposite wall, generating additional turbulent structures. Conversely, the behavior of

the cold jet differs from the patterns described above. In this case, the deformation of the turbulent structures is not a consequence of the interaction with the wall but rather results from the falling dynamics of the jet due to buoyancy. The turbulent structures become increasingly elongated along the jet axis in the lower part and show a finer appearance in the upper part. This observation is consistent with the description of the turbulent behavior of the experimental cold jet given earlier.

5. Conclusions

This paper presents a numerical study of axisymmetric and thermal jets generated by an air diffuser of complex design and developing near the ceiling of a full-scale test room with an original Lattice-Boltzmann-based Large-Eddy Simulation method (LBM-LES). An extensive validation procedure was conducted using a comprehensive dataset obtained from experimental measurements. The validation process involved a thorough examination of several physical parameters, such as mean velocity, temperature, and turbulence intensity fields, as well as the distribution of turbulence within the jets.

The findings of this study can be summarized as below:

1. The classical temperature wall function [54] has been adjusted by reducing the wall turbulence Prandtl number ($Pr_{t,w}$) to improve the prediction of convective heat transfer on walls in cases of mixed or natural convection.

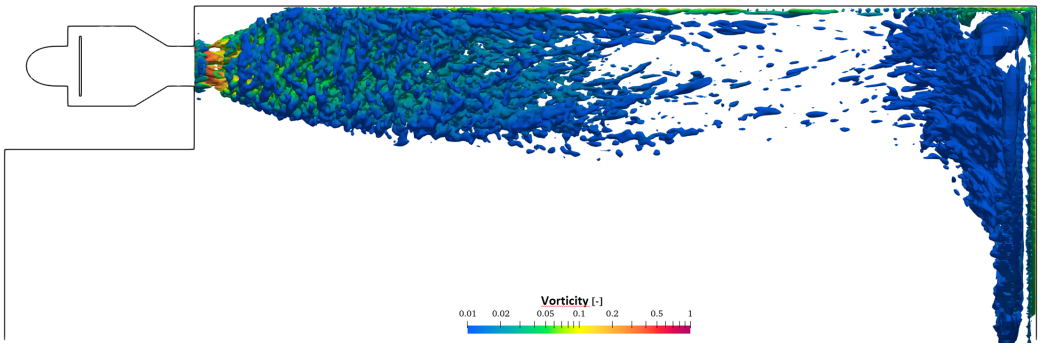

(a) Isothermal jet

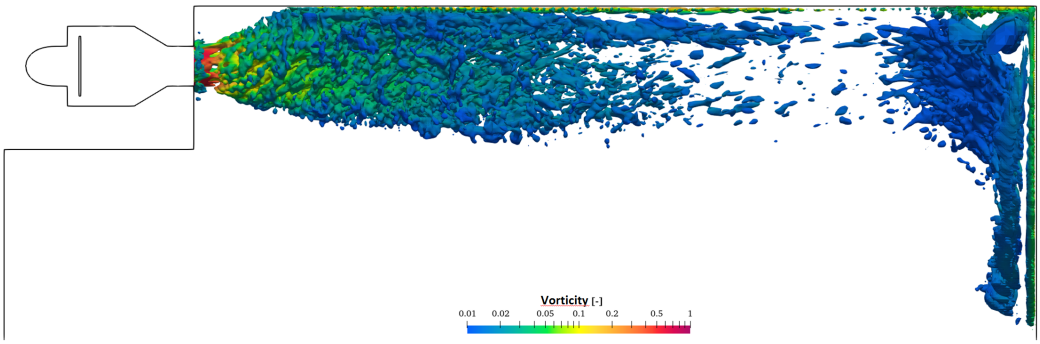

(b) Hot jet

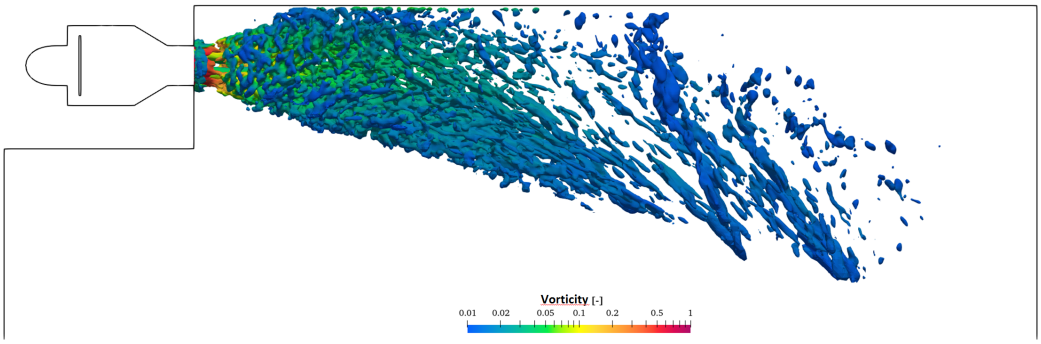

(c) Cold jet

Figure 14: Isosurfaces of Q-criterion from the mean field, coloured by the normalized vorticity and viewed from the side.

2. The adapted mesh resolution resulting from the grid convergence analysis study still require a high computational cost with a ratio of the wall-clock time to the physically simulated time of $1.85 \cdot 10^3$.
3. The mean velocity, temperature, and turbulence intensity profiles show good agreement with the experiments for the isothermal jet and the hot jet. In particular, a remarkable accuracy is observed on the temperature predicted at the room's central region, resulting from the temperature wall function adjustment. Some minor discrepancies were nonetheless observed, notably in the near-wall region. For the cold jet the results are satisfactory near the air inlet, but deviations were observed in the jet development zone with a slight overestimation of its vertical expansion.
4. Lumley triangles are used to characterize turbulence anisotropy by graphically representing the invariants of the Reynolds anisotropy tensor. The model can capture the main features of turbulence anisotropy, but has limitations in representing strongly anisotropic phenomena where turbulence converges to a one-dimensional state
5. The Q-criterion visualization effectively highlight the turbulent structures that develop within the jets.

Therefore, the LBM-LES approach is well-suited for building applications and can be applied more broadly to simulate thermal airflows within buildings. Coupling this model with a Building Energy Model would enable the consideration of more realistic dynamic boundary conditions at the walls

of the room, allowing for a detailed assessment of heat transfer dynamics and comfort. However, it would be beneficial to adopt a more appropriate near-wall thermal modeling approach for mixed convection, with a particular emphasis on directly incorporating the buoyancy effect. This approach would eliminate the need to adjust the classical thermal wall function that depends on $Pr_{t,w}$, which could potentially lead to improved heat transfer predictions at walls.

CRediT authorship contribution statement

Teddy Gresse: Data curation, Formal analysis, Investigation, Methodology, Visualization, Writing - Original Draft. **Lucie Merlier:** Methodology, Project administration, Supervision, Writing - Review & Editing. **Jérome Jacob:** Methodology, Software, Writing - Review & Editing. **Frederic Kuznik:** Conceptualization, Resources, Supervision, Writing - Review & Editing.

Declaration of Competing Interest

The authors declare that they have no known competing financial interests or personal relationships that could have appeared to influence the work reported in this paper.

Acknowledgments

The ProLB software used in this study is developed within a scientific collaboration including CS GROUP, Renault, Airbus, Safran, Ecole Centrale de Lyon, CNRS, and Aix-Marseille University. This work was granted access to the HPC resources of TGCC under the allocation 2022-A0132A13804 made by GENCI.

References

[1] M. González-Torres, L. Pérez-Lombard, J. F. Coronel, I. R. Maestre, D. Yan, A review on buildings energy information: Trends, end-uses, fuels and drivers, Energy Reports (2022). doi:10.1016/j.egyr.2021.11.280.

[2] B. Blocken, LES over RANS in building simulation for outdoor and indoor applications: A foregone conclusion?, Building Simulation 11 (2018) 821–870. doi:10.1007/s12273-018-0459-3.

[3] Q. Chen, Computational fluid dynamics for HVAC: successes and failures, ASHRAE Transactions 103 (1997) 178–187.

[4] Z. Zhai, Z. Zhang, W. Zhang, Q. Chen, Evaluation of Various Turbulence Models in Predicting Airflow and Turbulence in Enclosed Environments by CFD: Part-1: Summary of Prevalent Turbulence Models, HVAC&R Research (2007). doi:10.1080/10789669.2007.10391459.

[5] P. V. Nielsen, Fifty years of CFD for room air distribution, Building and Environment 91 (2015) 78–90. doi:10.1016/j.buildenv.2015.02.035.

[6] Q. Chen, J. Srebric, A procedure for verification, validation, and reporting of indoor environment CFD analyses, HVAC&R Research (2002). doi:10.1080/10789669.2002.10391437.

[7] D. Sorensen, P. Nielsen, Quality control of computational fluid dynamics in indoor environments, Indoor Air (2003). doi:10.1034/j.1600-0668.2003.00170.x.

[8] P. Nielsen, F. Allard, H. B. Awbi, L. Davidson, A. Schälin, Computational Fluid Dynamics in Ventilation Design REHVA Guidebook No 10, International Journal of Ventilation (2007).

[9] P. Nielsen, A. Restivo, J. Whitelaw, The velocity characteristics of ventilated room, ASME J. Fluids Engineering (1978). doi:10.1115/1.3448669.

[10] D. Blay, S. Mergui, C. Niculae, Confined Turbulent Mixed Convection in the Presence of a Horizontal Buoyant Wall Jet, Fundamentals of Mixed Convection (1992).

[11] J. D. Posner, C. R. Buchanan, D. Dunn-Rankin, Measurement and prediction of indoor air flow in a model room, Energy and Buildings 35 (2003) 515–526. doi:10.1016/S0378-7788(02)00163-9.

[12] J. Smagorinsky, General circulation experiments with the prim-

itive equations, Monthly Weather Review 91 (1963) 99–164. doi:10.1175/1520-0493(1963)091¡0099:GCEWTP¿2.3.CO;2.

[13] M. Germano, U. Piomelli, P. Moin, W. H. Cabot, A dynamic subgrid-scale eddy viscosity model, Physics of Fluids A: Fluid Dynamics (1991). doi:10.1063/1.857955.

[14] M. Wang, Q. Chen, Assessment of Various Turbulence Models for Transitional Flows in an Enclosed Environment, HVAC&R Research 15 (2009) 1099–1119. doi:10.1080/10789669.2009.10390881.

[15] A. Abdilghanie, L. Collins , D. Caughey, Comparison of Turbulence Modeling Strategies for Indoor Flows, Journal of Fluids Engineering 131 (2009). doi:10.1115/1.3112386.

[16] N. Morozova, F. X. Trias, R. Capdevila, C. D. Pérez-Segarra, A. Oliva, On the feasibility of affordable high-fidelity CFD simulations for indoor environment design and control, Building and Environment 184 (2020) 107144. doi:10.1016/j.buildenv.2020.107144.

[17] F. Kuznik, G. Rusaouën, R. Hohotă, Experimental and numerical study of a mechanically ventilated enclosure with thermal effects, Energy and Buildings 38 (2006) 931–938. doi:10.1016/j.enbuild.2005.08.016.

[18] Y. Sakamoto, Y. Matsuo, Numerical predictions of three-dimensional flow in a ventilated room using turbulence models, Applied Mathematical Modelling 4 (1980) 67–72. doi:10.1016/0307-904X(80)90216-4.

650 [19] L. Davidson, Large eddy simulation: A dynamic one-equation subgrid
651 model for three-dimensional recirculating flow, 11th International Sym-
652 posium on Turbulent Shear Flow (1997).

653 [20] W. Zhang, Q. Chen, Large eddy simulation of indoor airflow with a
654 filtered dynamic subgrid scale model, International Journal of Heat and
655 Mass Transfer 43 (2000) 3219–3231. doi:10.1016/S0017-9310(99)00348-
656 8.

657 [21] M. Su, C.-M. Chiang, Comparison of Different Subgrid-Scale Models
658 of Large Eddy Simulation for Indoor Airflow Modeling, Journal of Flu-
659 ids Engineering-transactions of The Asme - J FLUID ENG 123 (2001).
660 doi:10.1115/1.1378294.

661 [22] F. Kuznik, Étude expérimentale des jets axisymétriques anisother-
662 mes horizontaux se développant près d'une paroi : application à la
663 modélisation des cavités ventilées, Ph.D. thesis, INSA, Lyon, 2005.

664 [23] Z. F. Tian, J. Y. Tu, G. H. Yeoh, R. K. K. Yuen, Nu-
665 merical studies of indoor airflow and particle dispersion by Large
666 Eddy Simulation, Building and Environment 42 (2007) 3483–3492.
667 doi:10.1016/j.buildenv.2006.10.047.

668 [24] T. Kempe, A. Hantsch, Large-eddy simulation of indoor air flow using
669 an efficient finite-volume method, Building and Environment 115 (2017)
670 291–305. doi:10.1016/j.buildenv.2017.01.019.

[25] M. Auvinen, J. Kuula, T. Grönholm, M. Sühring, A. Hellsten, High-resolution large-eddy simulation of indoor turbulence and its effect on airborne transmission of respiratory pathogens - Model validation and infection probability analysis, Physics of Fluids (2022). doi:10.1063/5.0076495.

[26] T. Krüger, H. Kusumaatmaja, A. Kuzmin, O. Shardt, G. Silva, E. M. Viggen, The Lattice Boltzmann Method - Principles and Practice, springer ed., 2017. doi:10.1007/978-3-319-44649-3.

[27] B. Elhadidi, H. E. Khalifa, Comparison of coarse grid lattice Boltzmann and Navier Stokes for real time flow simulations in rooms, Building Simulation 6 (2013) 183–194. doi:10.1007/s12273-013-0107-x.

[28] A. Khan, N. Delbosc, C. Noakes, J. Summers, Real-time flow simulation of indoor environments using Lattice Boltzmann Method, Building Simulation (2015). doi:10.1007/s12273-015-0232-9.

[29] M. Han, R. Ooka, H. Kikumoto, Lattice Boltzmann method-based large-eddy simulation of indoor isothermal airflow, International Journal of Heat and Mass Transfer 130 (2018) 700–709. doi:10.1016/J.IJHEATMASSTRANSFER.2018.10.137.

[30] H. Sajjadi, M. Salmanzadeh, G. Ahmadi, S. Jafari, Simulations of indoor airflow and particle dispersion and deposition by the lattice Boltzmann

method using LES and RANS approaches, Building and Environment 102 (2016) 1–12. doi:10.1016/J.BUILDENV.2016.03.006.

[31] M. Jahidul Haque, M. Mamun Molla, M. Amirul Islam Khan, K. Ahsan, Graphics process unit accelerated lattice Boltzmann simulation of indoor air flow: Effects of sub-grid scale model in large-eddy simulation, Proceedings of the Institution of Mechanical Engineers, Part C: Journal of Mechanical Engineering Science 234 (2020) 4024–4040. doi:10.1177/0954406220919780.

[32] M. Han, R. Ooka, H. Kikumoto, Effects of wall function model in lattice Boltzmann method-based large-eddy simulation on built environment flows, Building and Environment 195 (2021) 107764. doi:10.1016/J.BUILDENV.2021.107764.

[33] M. Siodlaczek, M. Gaedtke, S. Simonis, M. Schweiker, N. Homma, M. J. Krause, Numerical evaluation of thermal comfort using a large eddy lattice Boltzmann method, Building and Environment 192 (2021) 107618. doi:10.1016/J.BUILDENV.2021.107618.

[34] M. Hu, Z. Zhang, M. Liu, Transient particle transport prediction based on lattice Boltzmann method-based large eddy simulation and Markov chain model, Building Simulation (2023). doi:10.1007/s12273-023-0995-3.

[35] F. Bazdidi-Tehrani, M. S. Sargazizadeh, Large eddy simulation of flow

field and particle dispersion in a ventilated model room using a parallel lattice Boltzmann method, Aerosol Science and Technology (2023). doi:10.1080/02786826.2023.2195464.

[36] CS, ProLB, http://www.prolb-cfd.com/, 2018.

[37] F. Kuznik, G. Rusaouën, J. Brau, Experimental Study of Turbulent Structures in a Non Isothermal Horizontal Jet Issuing from a Round Nozzle Distanced from a Wall, International Journal of Ventilation (2011). doi:10.1080/14733315.2011.11683955.

[38] F. Kuznik, J. Brau, Numerical and experimental investigation of a mechanically ventilated room: The impact of inlet boundary conditions on CFD modelling of the ventilation system, International Journal of Ventilation 4 (2005) 113–122. doi:10.1080/14733315.2005.11683703.

[39] F. Kuznik, G. Rusaouën, J. Brau, Experimental and numerical study of a full scale ventilated enclosure: Comparison of four two equations closure turbulence models, Building and Environment (2007). doi:10.1016/j.buildenv.2005.11.024.

[40] F. Kuznik, G. Rusaouën, J. Brau, Use of a RSM turbulence model for the prediction of velocity and temperature fields in a mechanically ventilated room, International Journal of Ventilation (2007). doi:10.1080/14733315.2007.11683774.

[41] F. Kuznik, J. Virgone, J. J. Roux, Energetic efficiency of room wall containing PCM wallboard: A full-scale experimental investigation, Energy and Buildings 40 (2008) 148–156. doi:10.1016/J.ENBUILD.2007.01.022.

[42] T. Gresse, L. Merlier, F. Kuznik, Detailed airflow dynamics and temperature data of axisymmetric and anisothermal jets developing in a room, Data in Brief 29 (2020) 105382. doi:10.1016/j.dib.2020.105382.

[43] P. L. Bhatnagar, E. P. Gross, M. Krook, A Model for Collision Processes in Gases. I. Small Amplitude Processes in Charged and Neutral One-Component Systems, Physical Review (1954). doi:10.1103/PhysRev.94.511.

[44] J. Jacob, O. Malaspinas, P. Sagaut, A new hybrid recursive regularised Bhatnagar–Gross–Krook collision model for Lattice Boltzmann method-based large eddy simulation, Journal of Turbulence (2018) 1–26. doi:10.1080/14685248.2018.1540879.

[45] Z. Guo, C. Zheng, B. Shi, Discrete lattice effects on the forcing term in the lattice Boltzmann method, Physical Review E (2002). doi:10.1103/PhysRevE.65.046308.

[46] Y. Feng, P. Boivin, J. Jacob, P. Sagaut, Hybrid recursive regularized lattice Boltzmann simulation of humid air with application to meteorological flows, Physical Review E (2019). doi:10.1103/PhysRevE.100.023304.

[47] P. Lallemand, L. Luo, Hybrid finite-difference thermal lattice Boltzmann equation, International Journal of Modern Physics B (2003). doi:10.1142/S0217979203017060.

[48] Y. Chen, H. Ohashi, M. Akiyama, Thermal lattice Bhatnagar-Gross–Krook model without nonlinear deviations in macrodynamic equations, Physical Review E (1994).

[49] X. He, S. Chen, G. D. Doolen, A Novel Thermal Model for the Lattice Boltzmann Method in Incompressible Limit, Journal of Computational Physics 146 (1998) 282–300. doi:10.1006/JCPH.1998.6057.

[50] A. W. Vreman, An eddy-viscosity subgrid-scale model for turbulent shear flow: Algebraic theory and applications, Physics of Fluids 16 (2004) 3670–3681. doi:10.1063/1.1785131.

[51] S. Wilhelm, J. Jacob, P. Sagaut, An explicit power-law-based wall model for lattice Boltzmann method-Reynolds-averaged numerical simulations of the flow around airfoils, Physics of Fluids 30 (2018). doi:10.1063/1.5031764.

[52] N. Afzal, Wake Layer in a Turbulent Boundary Layer with Pressure Gradient: A New Approach, IUTAM (1996) 95–118. doi:10.1007/978-94-009-1728-6_9.

[53] S. G. Cai, P. Sagaut, Explicit wall models for large eddy simulation, Physics of Fluids 33 (2021). doi:10.1063/5.0048563.

[54] B. A. Kader, Temperature and concentration profiles in fully turbulent boundary layers, International Journal of Heat and Mass Transfer 24 (1981) 1541–1544. doi:10.1016/0017-9310(81)90220-9.

[55] P. Kiš, H. Herwig, The near wall physics and wall functions for turbulent natural convection, International Journal of Heat and Mass Transfer 55 (2012) 2625–2635. doi:10.1016/J.IJHEATMASSTRANSFER.2011.12.031.

[56] T. Zhang, H. Zhou, S. Wang, An adjustment to the standard temperature wall function for CFD modeling of indoor convective heat transfer, Building and Environment 68 (2013) 159–169. doi:10.1016/J.BUILDENV.2013.06.009.

[57] Y. Zhu, Q. Ouyang, B. Cao, X. Zhou, J. Yu, Dynamic thermal environment and thermal comfort, Indoor Air 26 (2015) 125–137. doi:10.1111/ina.12233.

[58] J. L. Lumley, Computational Modeling of Turbulent Flows, volume 18, 1979. doi:10.1016/S0065-2156(08)70266-7.

[59] S. B. Pope, Turbulent Flow, Cambridge University Press, 2000. doi:10.1017/CBO9780511840531.